Macrophage phenotype transitions in a stochastic gene-regulatory network model

Anna-Simone Josefine Frank [a,*], Kamila Larripa [b], Hwayeon Ryu [c], Susanna Röblitz [a]

[a] Computational Biology Unit, Department of Informatics, University of Bergen, Bergen, Norway
[b] Department of Mathematics, California State Polytechnic University Humboldt, Arcata, CA, USA
[c] Department of Mathematics and Statistics, Elon University, Elon, NC, USA

ARTICLE INFO

ABSTRACT

Polarization is the process by which a macrophage cell commits to a phenotype based on external signal stimulation. To know how this process is affected by random fluctuations and events within a cell is of utmost importance to better understand the underlying dynamics and predict possible phenotype transitions. For this purpose, we develop a stochastic modeling approach for the macrophage polarization process. We classify phenotype states using the Robust Perron Cluster Analysis and quantify transition pathways and probabilities by applying Transition Path Theory. Depending on the model parameters, we identify four bistable and one tristable phenotype configuration. We find that bistable transitions are fast but their states less robust. In contrast, phenotype transitions in the tristable situation have a comparatively long time duration, which reflects the robustness of the states. The results indicate parallels in the overall transition behavior of macrophage cells with other heterogeneous and plastic cell types, such as cancer cells. Our approach allows for a probabilistic interpretation of macrophage phenotype transitions and biological inference on phenotype robustness. In general, the methodology can easily be adapted to other systems where random state switches are known to occur.

1. Introduction

Macrophages are a specific type of immune cells (Lahmar et al., 2016). In a process called polarization macrophages adopt different phenotypes in response to external signals and their microenvironment. Such stimulation results in a continuum of macrophage phenotype variety and functionality that has been simplified into a dichotomous framework: on one end, there are classically activated (M1-phenotype) macrophages and on the other end alternatively activated types (M2-phenotype). M1-like macrophages are pro-inflammatory and direct host defense, whereas M2-like macrophages have quite the opposite effect—they resolve inflammation and repair tissue (Mantovani et al., 2005). The original dichotomous framework is based on in vitro studies in which macrophages were stimulated with IFN-γ or IL-4 to induce an M1 or M2 phenotype, respectively (Martinez and Gordon, 2014). In between these extremes, unique or mixed phenotypes have been observed (Sica and Mantovani, 2012), particularly in pathological contexts such as neurodegenerative disorders (Garofalo et al., 2003) or the tumor microenvironment (Biswas et al., 2008).

Macrophage polarization is regulated by cytokine signals which induce the Jak-STAT pathway in these cells (Hu et al., 2007). This pathway communicates information from chemical signals outside of a cell to the nucleus, resulting in the activation of genes. Binding of the ligand (e.g., a cytokine) to its cell-surface receptor activates JAK proteins, which then self-phosphorylate and then phosphorylate their associated receptor. This action recruits STATs which are phosphorylated by the JAKs to form a dimer. The dimer translocates from the cytosol to the cell nucleus to induce transcription of target genes (O'Shea and Plenge, 2012). This pathway is ubiquitous in the cell and has roles in development, immunity, and cancer. It also integrates with other cell signaling pathways (e.g. mTOR and MAPK/ERK). Its role in cytokine receptor signaling is one of its many purposes. In the context of macrophages, IFN-γ induced STAT1 activation facilitates the transcription of genes which create pro-inflammatory products (Ma et al., 2020) whereas IL-4 induced STAT6 activation has the opposite effect (Waqas et al., 2019) and represses inflammatory markers in macrophages (Czimmerer et al., 2018). Within the binary phenotype classification system, simultaneous high STAT1 and low STAT6 activation is interpreted as the
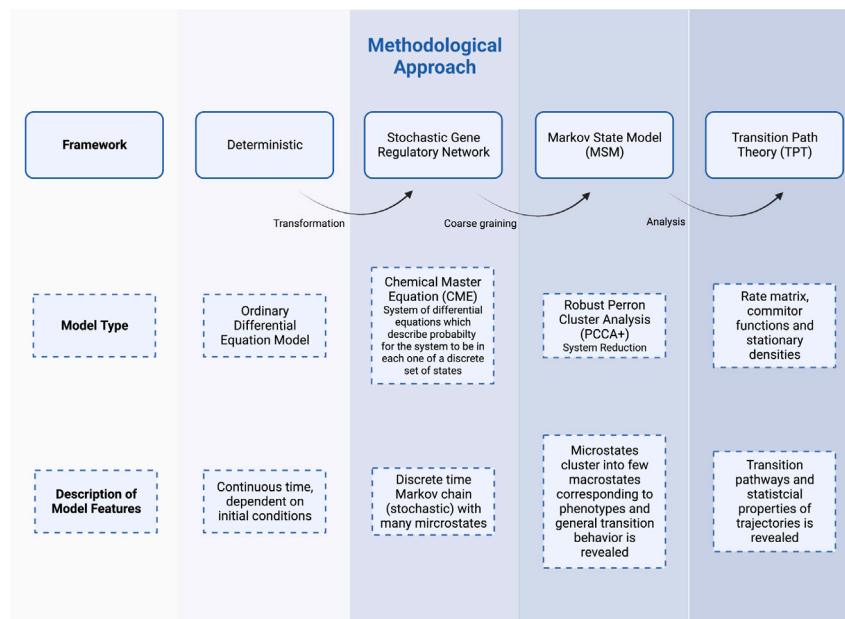

Fig. 1. Flowchart of the methodological approach. First, a deterministic model of macrophage polarization is transformed into a stochastic modeling framework. We then use a clustering approach to identify possible multistable phenotypes based on several different parameter sets. Finally, to calculate phenotype transition paths and probabilities between the identified phenotypes, we apply Transition Path Theory. Created with Biorender.com.

M1 phenotype, whereas reversed activation levels characterize the M2 phenotype (Bardi et al., 2018). While we acknowledge that the binary classification of macrophage phenotypes into a M1 and M2 category is oversimplified, we use this terminology to make our results more easily comparable with the current literature and reflect the historical in vitro experiments related to macrophage polarization in which a macrophage is stimulated with a single cytokine to induce polarization.

We also know that macrophages within a tumor can switch between phenotypes, which determine their functionality to be either promoting or suppressing tumor growth (Poh and Ernst, 2018). In other words, macrophages are very plastic cells (Biswas and Mantovani, 2010) that can reverse their activation state fully and rapidly. Therefore, a given macrophage may participate sequentially in the induction and resolution of inflammation (Porcheray et al., 2005).

Even with this biological insight, knowledge gaps exist in understanding how microenvironmental signaling drives polarization, phenotype switching and functionality, and ultimately pathological outcomes. To address these knowledge gaps, several deterministic model frameworks, based on Ordinary Differential Equations (ODEs), have been developed in recent years to better understand macrophage polarization processes, and the transitions between phenotypes, e.g., Nickaeen et al. (2019), Smith et al. (2016), Zhao et al. (2019), Frank et al. (2021). These models confirmed the existence of already known phenotypes, and predicted others not yet described in the literature. Furthermore, bifurcation analysis revealed the possibility of phenotype switches that are known to exist in living cells and cell cultures (Sica and Mantovani, 2012).

Deterministic model frameworks build on the assumption that there are a large number of molecules (e.g., transcription factors) present within a cell. Contrary to this assumption, (human) cells may include only a restricted number of molecule copies, such that intrinsic noise and random fluctuations play an important role. Therefore, frameworks exist to study stochastic gene-regulatory networks of cell-fate decisions, such as energy landscape analysis (Coomer et al., 2022; Ye et al., 2021), or transition path theory (Li et al., 2021; Lang et al., 2021). Such approaches help identify possible important pathways and respective probabilities of phenotype switches, along with the responsible underlying mechanisms.

In this paper, we aim to mimic a stochastic cell environment by taking into account randomness within a single macrophage cell. Using the Markov state modeling (MSM) framework, we first study possible phenotype configurations and compare them to the outcome of deterministic model approaches. Then, applying transition path theory (TPT), we analyze the transition routes of the identified phenotypes and their corresponding probabilities. Recently, a similar approach has been applied in describing lysis-lysogeny transition and stem cell development (Li et al., 2021).

The article is organized in the following way. We start with the presentation of the methodological approach in Section 2, followed by the results in Section 3, and end with their discussion in Section 4. Appendix includes more details on the methods, additional figures and tables describing our results. Matlab code (macro-tpt Frank and Röblitz (2022)) to reproduce the results from this paper is available from https://github.com/a-sfrank/macro-tpt.git.

2. Methods

An overview of the methodological approach used in this article is presented in Fig. 1.

2.1. The deterministic ODE model

We start with a deterministic ODE model that describes dynamic changes of STAT1 and STAT6 in a single macrophage (Frank et al., 2021). This model is characterized by an asymmetry in the regulatory mechanisms and exhibits complex dynamics in terms of multistability. A graphical representation of the model is shown in Fig. 2. The variable x_1 represents STAT1, a marker for M1 polarization, and the variable x_2 represents STAT6, a marker for M2 polarization, along with two input signals (denoted by S_1 and S_2). The equations of the ODE model are

$$x_1' = \left(a_1 \cdot H^+(x_1, k_1, n_1) + S_1\right) \cdot H^-(x_2, p_2, l_2) + b_1 - q_1 x_1, \tag{1}$$

$$x_2' = a_2 \cdot H^+(x_2, k_2, n_2) + S_2 \cdot H^-(x_1, p_1, l_1) + b_2 - q_2 x_2, \tag{2}$$

where $' = d/dt$. The term $H^+(x_i, k_i, n_i) = x^{n_i}/(x^{n_i} + k_i^{n_i})$ denotes a stimulatory Hill function, whereas $H^-(x_i, p_i, l_i) = p_i^{l_i}/(p_i^{l_i} + x_i^{l_i})$ denotes an inhibitory Hill function. For more details on the ODE model construction, see Frank et al. (2021). The model parameters and their descriptions are provided in Table 1.
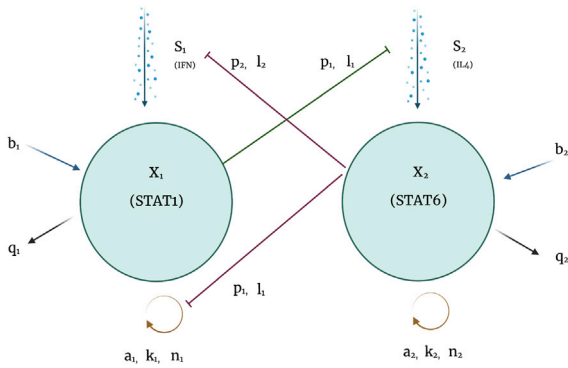
Fig. 2. Schematic diagram of the modeled signaling network. The variable x_1 represents STAT1, a marker for M1 polarization, and the variable x_2 represents STAT6, a marker for M2 polarization, along with two input signals (denoted by S_1 and S_2). Self-stimulation of STATs ($a_i, n_i, k_i, i \in \{1, 2\}$) is represented by the orange loops at the bottom of the figure, while processes of mutual-inhibition are depicted with red and green inhibiting lines ($p_i, l_i, i \in \{1, 2\}$). The incoming blue arrows ($b_i, i \in \{1, 2\}$) represent basal activation of STATs which also occurs in the absence of cytokine signaling. The outgoing black arrows ($q_i, i \in \{1, 2\}$) represent deactivation of STATs. Incoming arrows at the top represent cytokine signaling (IFN (S_1) and IL4 (S_2) respectively). Note the asymmetry in that STAT6 inhibits both the input signal and self stimulation of STAT1, but STAT1 impacts only the input signal for STAT6. See Frank et al. (2021) for a detailed description of the model equations. Created with Biorender.com.
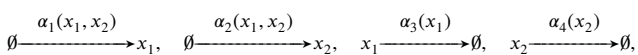
Table 1
Model parameters in Eqs. (1)–(2).

Parameter	Description
$a_{1,2}$	Strength of self-stimulation
$b_{1,2}$	Basal activation rates
$n_{1,2}$	Exponents in the Hill functions for self-stimulation
$k_{1,2}$	Thresholds in the Hill functions for self-stimulation
$l_{1,2}$	Exponents in the Hill functions for mutual inhibition
$p_{1,2}$	Thresholds in the Hill function for mutual inhibition
$q_{1,2}$	Deactivation rates
$S_{1,2}$	Input signal strength

2.2. Building the stochastic gene-regulatory network model

The Chemical Master Equation (CME) is a fundamental description of stochastic chemical kinetics commonly used to model noisy gene regulatory networks. It takes into account random fluctuations in the time points and the order of chemical reactions. The CME is a system of differential equations that describes the evolution of *probability densities* in the state space. For a system involving D different species, the state space is $\mathbb{N}^D$, i.e., the space of D-dimensional positive integer vectors containing the copy-numbers of each of the D species. The CME can usually only be solved numerically, which is a tedious task. Alternatively, one can draw sample realizations of the underlying stochastic Markov jump process by using the stochastic simulation algorithm (SSA) (Gillespie, 1976).

In order to derive the CME from the deterministic ODE model, the ODE system is first decomposed into four elementary reactions corresponding to synthesis and degradation of STAT1 and STAT6, respectively,

$$\emptyset \xrightarrow{\alpha_1(x_1, x_2)} x_1, \quad \emptyset \xrightarrow{\alpha_2(x_1, x_2)} x_2, \quad x_1 \xrightarrow{\alpha_3(x_1)} \emptyset, \quad x_2 \xrightarrow{\alpha_4(x_2)} \emptyset,$$

with the four stochastic propensity functions

$$\alpha_1(x_1; x_2) = \left(a_1 \cdot H^+(x_1, k_1, n_1) + S_1\right) \cdot H^-(x_2, p_2, l_2) + b_1,$$
$$\alpha_2(x_1; x_2) = a_2 \cdot H^+(x_2, k_2, n_2) + S_2 \cdot H^-(x_1, p_1, l_1) + b_2,$$
$$\alpha_3(x_1) = q_1 \cdot x_1,$$
$$\alpha_4(x_2) = q_2 \cdot x_2,$$

and stoichiometric change matrix

$$S = \begin{pmatrix} 1 & 0 & -1 & 0 \\ 0 & 1 & 0 & -1 \end{pmatrix}.$$

Denote by $p(i, j)$ the probability to find the system in state ($x_1 = i, x_2 = j$) at time t. The CME is the balance equation for the change in this probability density:

$$\frac{d}{dt} p(i, j) = \alpha_1(i - 1, j) \cdot p(i - 1, j) + \alpha_3(i + 1) \cdot p(i + 1, j)$$
$$+ \alpha_2(i, j - 1) \cdot p(i, j - 1) + \alpha_4(j + 1) \cdot (i, j + 1)$$
$$- \left[\alpha_1(i, j) + \alpha_3(i) + \alpha_2(i, j) + \alpha_4(j)\right] \cdot p(i, j)$$

If the state space is truncated and enumerated with states $k = 1, 2, \ldots, n$, this equation can be written in matrix notation,

$$p' = Q \cdot p, \quad p \in \mathbb{R}^n, \ Q \in \mathbb{R}^{n \times n} \tag{3}$$

whereby the transition rate matrix Q has column sums zero. The stationary density $\pi \in \mathbb{R}^n$ is given by the eigenvector of Q corresponding to eigenvalue $\lambda = 0$,

$$Q \cdot \pi = 0. \tag{4}$$

2.3. Phenotype identification via clustering

Stochastic changes in particular patterns of gene expression have been identified with spontaneous phenotype transitions that can diversify otherwise identical cell-populations. These gene expression patterns correspond to metastable regions in the state space of the CME. The dynamics remains in these regions for a long time before it rapidly switches to another metastable region.

Multistability is characterized by the occurrence of a cluster of $n_c > 1$ eigenvalues $\lambda_1 = 0 > \lambda_2 > \cdots > \lambda_{n_c}$ close to zero for the matrix Q. Note that the eigenvalue $\lambda_1 = 0$ is equivalent to the Perron root $\lambda_1 = 1$ (also called the leading eigenvalue or dominant eigenvalue) of the corresponding transition probability matrix $P(\tau) = \exp(\tau \cdot Q)$. It has been demonstrated previously (Röblitz and Weber, 2013) that the subspace spanned by the corresponding eigenvectors, X, contains all information about the location of the metastable regions. To extract this information, spectral clustering approaches, such as the Robust Perron Cluster Analysis (PCCA+) (Röblitz and Weber, 2013), are useful. The PCCA+ computes a transformation matrix A such that the transformed eigenvectors $\chi = X \cdot A$ become so-called membership vectors. These membership vectors form a fuzzy clustering of the state space in that they assign to any state the probabilities for belonging to any of the n_c clusters, which represent the metastable regions. In the context of macrophage polarization, the metastable regions define the different phenotypes.

Furthermore, the membership vectors are used to project (coarse grain) the dynamics onto the space of metastable regions by

$$Q_c = (\chi^T \cdot \text{diag}(\pi) \cdot \chi)^{-1} \cdot \chi^T \cdot \text{diag}(\pi) \cdot Q \cdot \chi = A^{-1} \cdot \text{diag}(\lambda) \cdot A,$$

where $\lambda = (\lambda_1, \ldots, \lambda_{n_c})$. The statistical weights w_k of the clusters can be computed by

$$w_k := \chi_k^T \pi, \quad k = 1, \ldots, n_c.$$

Similarly, the normalized partial densities of the clusters are given by

$$\pi_k := \text{diag}(\pi) \cdot \chi_k / w_k.$$

While the coarse grained transition rates might be difficult to interpret, the corresponding coarse grained transition probabilities for a time interval of length τ can be obtained via the matrix exponential

$$P_c(\tau) = \exp(\tau \cdot Q_c).$$

If not stated otherwise, we use $\tau = 100$ throughout the computations. This reduced representation of the dynamics as transition probability matrix of a low-dimensional Markov chain is referred to as *Markov state model*.

2.4. Choice of parameter sets

With no background knowledge about adequate model parameters leading to multistability in the stochastic model, we relied on the parameter sets presented in the ODE model (Frank et al., 2021), which give rise to bi-, tri- and quadstability in the deterministic case. These parameter values were adapted from an empirical T-cell model (Yates et al., 2004) and are considered biologically reasonable.

The dimension of x_1 (STAT1) and x_2 (STAT6) in the ODE model is concentration. Hence, we need to multiply all parameters that contain units of concentration (i.e., $a_1, a_2, b_1, b_1, k_1, k_2, p_1, p_2, S_1, S_2$) with a factor that accounts for the conversion from concentrations to molecular copy numbers. If the unit of x_1 and x_2 was mol/L (molar, M), this conversion requires multiplication with both the volume (in litre) as well as Avogadro's constant $n_A = 6 \cdot 10^{23}$ (number of molecules in one mol). If the unit of x_1 and x_2 was in a different concentration unit, e.g., pM or nM, then a third factor is required that accounts for conversion from any concentration unit to mol/L. At the end, it is only the lump factor that occurs as parameter in the CME model, and the important fact is that this factor is proportional to the system volume.

This conversion follows the approach taken by Vellela and Qian (2009). They derive the CME from the ODE as a birth–death process, whereby the rates in the stochastic model are related to the rates in the deterministic model by a factor of the volume parameter V which depends on the order of the reaction. The authors consider values of 20, 40, and 80 in their numerical analysis. A factor $V = 6$ would convert, for example, a concentration of 1 pM into 6 molecular copy numbers in a volume of 10 pL. The order of magnitude of this factor seems to be reasonable, given that the typical volume of a human alveolar macrophage is in the pico-litre range (Krombach et al., 1997) and typical protein concentrations in a cell in the pico- to low nano-molar range (Wenta et al., 2008; González Pérez et al., 2009).

In our simulations, we use a conversion factor $V = 12.9$ and multiply the concentration-related parameters from (Frank et al., 2021) with this factor. The authors in Vellela and Qian (2009) demonstrate that the conversion factor V is a critical parameter. In their numerical example, increasing its value leads to a change in peak heights in the bistable stationary distribution. We therefore varied V to see how it influences the multistability patterns.

Generally, there is no one-to-one correspondence between the dynamics of the ODE and that of the CME model. Hence, it is not surprising that the CME model with the transformed parameter sets did not result in the same multistability as the ODE model. We therefore varied some of the stochastic model parameters that were identified as being most sensitive in the ODE model (Frank et al., 2021), e.g., $q_{1,2}, k_{1,2}, S_{1,2}, a_2$, whenever the parameter transformation did not result in the expected multistability in the stochastic model. Hence, the primary rationale behind this variation was to find parameter sets that lead to multistability in our stochastic model. To asses whether parameter sets result in multistability, we used three different criteria: (i) the gap in the *zero* eigenvalue spectrum of the transition rate matrix Q, (ii) the quality of the clustering (the crispness of the membership functions χ), and (iii) the spatial separation of the resulting metastable regions. We selected parameter sets for presentation that satisfy all three conditions.

2.5. Computing phenotype transition paths and probabilities

Transition Path Theory (TPT) has originally been developed in the context of molecular dynamics simulations, but has previously also been applied to gene regulatory networks (Chu et al., 2017; Tse et al., 2018). The theory is described in detail in numerous papers (Metzner et al., 2009; Noé et al., 2009; Vanden-Eijnden, 2010).

Based on the identified macrophage phenotypes, TPT is applied to determine the transition pathways along which macrophages switch their phenotype, together with the corresponding path probabilities.

For completeness, we briefly summarize the TPT concepts that are important for our application to macrophage polarization, but refer the reader to Appendix A.1, as well as the above mentioned papers for more details.

TPT takes as input the transition rate matrix $Q = (\ell_{ij})_{i,j \in S} = Q(i,j)_{i,j \in S}$ (from Eq. (3)) of a Markov jump process $\{X\}_{t \in \mathbb{R}}$ defined on a discrete state space S. Based on the assumption that the process $\{X\}_{t \in \mathbb{R}}$ is irreducible and ergodic, the time-reversed process $\{\tilde{X}\}_{t \in \mathbb{R}}$ is also a Markov jump process with a rate matrix $\tilde{Q} = (\tilde{\ell})_{i,j \in S}$ given by $\tilde{\ell}_{i,j} = \frac{\pi_j}{\pi_i} \ell_{ji}$ (Metzner et al., 2009), where π is the invariant distribution (or stationary density) of both processes $\{X\}_{t \in \mathbb{R}}$ and $\{\tilde{X}\}_{t \in \mathbb{R}}$, satisfying Eq. (4).

TPT is based on *reactive trajectories*, which are defined as transitions between two non-empty, disjoint subsets A and B of the state-space S, where one set is the source and the other one is the sink state (Noé et al., 2009; Metzner et al., 2009).

As a first step, we compute the discrete forward q^+ and backward q^- committor functions, as they are essential to calculate statistical properties and dynamical information of the reactive trajectories. q^+ is the probability that the process that starts in $i \in S$ will first reach subset B rather than A, while q^- describes the probability that the process first visited sub-set A rather than B (Metzner et al., 2009). In a second step, we calculate statistical properties that allow for a dynamical interpretation of the ensemble of reactive trajectories between subsets A and B in the state space S (Helfmann et al., 2020). Table A.3 summarizes important measures in TPT to describe dynamical information and states the corresponding interpretation. For the detailed computation of these quantities, the reader is referred to Appendix A.1.

In a third step, we coarse-grain the probability current of reactive trajectories, f_{ij}^{AB}, by projecting it onto the metastable state regions S_i and S_j from the Markov State Model, i.e., onto the phenotypes,

$$\tilde{F}_{S_i \to S_f} = \sum_{k \in S_i, l \in S_f} f_{k,l}^{AB}, \tag{5}$$

which in its normalized form reads

$$p_{S_i \to S_f}^r = \frac{\tilde{F}_{S_i \to S_f}}{\sum_{i=S_i, f \neq S_i} \tilde{F}_{S_i \to S_f}}. \tag{6}$$

In this step, we define a set S_k as the support of a partial density π_k in such a way that it carries at least $(1 - \varepsilon) \cdot 100\%$ of this density, i.e.

$$\sum_{i \in S_k} \pi_k(i) > 1 - \varepsilon,$$

whereby we choose $\varepsilon = 10^{-8}$.

Finally, by using probability tree diagrams, the relative probabilities of the path segments $p_{S_i \to S_f}^r$ are combined along an individual pathway P_i from A to B to define the *total relative probability p_i^r of path P_i*.

3. Results

3.1. Parameter sets for multistability

Following the procedure described in Section 2.4, we identified five different parameter sets (cases) that lead to different combinations of phenotypes. These are presented in Table 2.

Parameter sets leading to bi- and tristability are notably different from each other. For example, the phenotype observation in case 1 is driven by the parameter ratio of $b_1 \gg b_2$, and partly by $q_1 > q_2$. Tristability (case 5) results from bistability (case 2) by increasing the external input signals $S_{1,2}$. Other bistable cases (e.g., case 3 and 4) emerge, respectively, from parameter cases 2 and 1 by a change of values in a_1, b_1, q_2 and $S_{1,2}$. These parameter dependencies potentially reflect the differences in cellular conditions driving phenotype emergence.

Table 2
Parameter sets. The table presents the five different cases of parameter sets from the manual sampling approach, which give rise to multistable macrophage phenotypes in the stochastic model. The values are based on the model parameters in Frank et al. (2021). Due to the conversion to molecule numbers, parameters $a_{1,2}$, $b_{1,2}$, $k_{1,2}$, $p_{1,1}$ and $S_{1,2}$ have to be multiplied with the factor $u \cdot V \cdot n_A = 12.9$.

Parameters	a_1	a_2	b_1	b_2	n_1	n_2	k_1	k_2	l_1	l_2	p_1	p_2	q_1	q_2	S_1	S_2
Case 1 (bi)	5	5	15	0.05	6	6	1	1	1	1	0.5	1	5	1	2	0.155
Case 2 (bi)	15	5	0.05	0.05	6	6	1	1	1	1	0.5	1	5	1	2	0.155
Case 3 (bi)	15	5	0.05	0.05	6	6	1	1	1	1	0.5	1	5	5	1	0.0775
Case 4 (bi)	5	5	0.001	0.05	6	6	1	1	1	1	0.5	1	5	1	2	0.155
Case 5 (tri)	15	5	0.05	0.05	6	6	1	1	1	1	0.5	1	5	1	0.31	0.024

3.2. Identified phenotypes in the stochastic environment

We observe diversity in multistable macrophage phenotype configurations, specifically bi- and tristability, as presented by the clustering results in Table A.4. Multistability is also visible in the corresponding transition probability matrices P_c and the surface plots of the partial densities, which represent the multiple phenotypes states (see Fig. 3 for bistability and Fig. A.6 for tristability).

Depending on parameters used in the model (see Table 2), Fig. 3 shows four different pairs of bistable phenotype sets, which are defined based on the relative levels (i.e., low, high) of activation in x_1/x_2: (1) high x_1/low x_2 (H/L) and high x_1/high x_2 (H/H) in Fig. 3(a), (2) low x_1/high x_2 (L/H) and high x_1/low x_2 (H/L) in Fig. 3(c), (3) low x_1/low x_2 (L/L) and high x_1/low x_2 (H/L) in Fig. 3(e) and (4) low x_1/low x_2 (L/L) and low x_1/high x_2 (L/H) in Fig. A.7(g). Only one tristable case was detected, which comprised the L/L, the H/L and the L/H phenotypes (see Fig. A.6).

Furthermore, the statistical weights w_i ($i = 1, 2, 3$) in Table A.4 indicate how much time the dynamical process spends in a specific phenotype region before switching to another one. The higher the weight, the longer the expected holding time.

3.3. Phenotype transitions in the bistable case

The dynamic flow paths between the phenotypes are presented in Figs. 3 and A.7.

The information above and in Table A.5 reveals that for the parameter set in case 4 (see Table 2), a macrophage will never transition directly from L/L to L/H or vice-versa but will always pass through the complement set (C) when making this phenotype change. However, in case 3, the transition probabilities indicate that a macrophage is much more likely to directly transition between L/L and H/L rather than meander through a complement set. Additionally, the transition time can be compared between different cases (see Table A.5). For example, it is an order of magnitude faster for a macrophage to transition from L/L to H/L in Case 3 rather than from H/L to L/L.

Overall, the transitions happen mostly (with nearly 100%) on one specific path, directly from the start to the end set, through the complement set (C). This observation is different from what we observe when there are more than two phenotypes present, as discussed for the tristable case in the following.

3.4. Phenotype transitions and probabilities in the tristable case

The dynamic flow paths between the three identified phenotypes (L/L, H/L and L/H) are presented in Figs. 4 and A.8 for different combinations of start and end phenotype. They were generated from the parameter set in case 5 (Table 2).

The transition networks are illustrated in Figs. 4(b), Fig. 4(d), Fig. 4(f), and Fig. 4(h) as well as in Figs. A.8(b) and Fig. A.8(d). As it can be seen from these figures, the choice of start and end set plays an important role for the transition dynamics and phenotype realizations of the macrophage cell. This choice influences the specific transition

paths and their probabilities. In the following, we therefore distinguish between the different flow directions by enumerating them as 'subcases 1–6'.

In subcase 1, the states L/H and H/L are the end sets and L/L is the start set (see Figs. A.8(a) and Fig. A.8(b)), while in subcase 2 the start set is defined as the combination of the L/L and H/L phenotype (see Figs. A.8(c) and Fig. A.8(d)). In these two cases, we observe short transition times ($t = 0.16$ and 0.40, respectively) (see Table A.6) with high transition probabilities for the different paths. Particularly, subcase 1 shows that cells are more likely to end up in the H/L phenotype (57.4%) than in the L/H phenotype (43.6%). In subcase 2, 90.3% of the transitions to the L/H state start in the L/L phenotype, while only 9.6% start in the H/L state.

Both subcases 3 and 4 start from the same start set (L/L), but their end phenotype as well as the intermittent phenotype differ (see Figs. 4(a) and 4(c)). For example, in subcase 4 macrophage cells coming from the L/L state end up with 99.2% probability in the H/L phenotype (either directly or via the complement, see Table A.6). There is, however, an additional very small probability that the macrophage switches to the L/H phenotype, and stays there for a very long time, before settling in the final H/L state. The stopover in the L/H state is represented by the self-loop in the corresponding transition network (see Fig. 4(d)). This discourse over the L/H phenotype, with a very low segment probability (3.8e−6%) of leaving the state (L/H), makes the transition from the L/L to the H/L phenotype lasting very long on average ($t = 135337$) and thus very unlikely (see Table A.6). Similar interpretations can be drawn for subcase 3 based on the presented results in Figs. 4(a) and 4(b) and the Table A.6. Here, however, the results indicate that the macrophage cell is able to leave the intermittent state (H/L). This is also indicated by the relatively fast transition time ($t = 2.03$).

Similar to subcase 4, also subcases 5 and 6 represent a situation where the final phenotype state will probably not be reached. Here, the start sets are the L/H, respectively the H/L phenotype, and the end sets are the H/L and L/H phenotype, respectively (see Figs. 4(e) and 4(g)). The dynamic information in Table A.6, as well as the segment probabilities in the corresponding transition networks in Figs. 4(f) and 4(h) indicate that the transition flow is recurrently drawn towards the intermittent phenotype state (I) with high probability (i.e., there are path segments with a very low probability for leaving the intermittent state, while the probabilities of path segments leading to this state are high). In other words, it will require several transition iterations between the intermittent state (I) and the complement set (C) until the end state is reached. This observation can also be inferred from the low probabilities of the respective transition paths (see Table A.6). The average length of a successful transition in cases 5 and 6 ($t = 699$ and $t = 1359$, respectively, see Table A.6) reflects this result as well.

3.5. Influence of volume scaling on multistability

As mentioned in Section 2.4, the conversion factor V is a critical parameter. We therefore analyzed how multistability is affected if V is varied for one of the cases. Fig. 5 shows how the stationary density

(a) Case 1: H/H and H/L phenotype

(b) Case 1: Transitions (grey) from H/H (red) to H/L (blue)

(c) Case 2: H/L and L/H phenotype

(d) Case 2: Transitions (grey) from H/L (red) to L/H (blue)

(e) Case 3: L/L and H/L phenotype

(f) Case 3: Transitions (grey) from L/L (red) to H/L (blue)

(g) Case 4: L/L and L/H phenotype

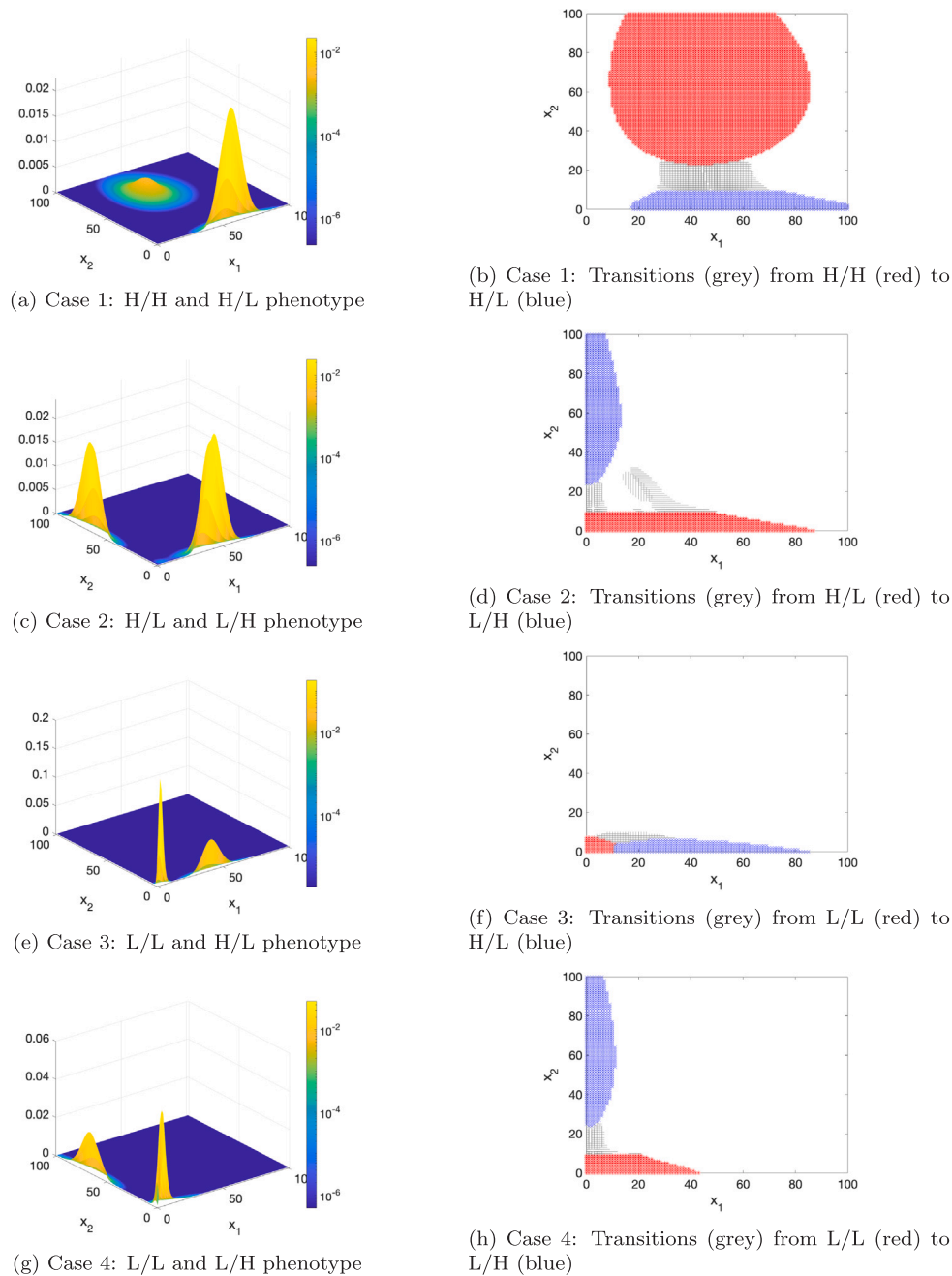(h) Case 4: Transitions (grey) from L/L (red) to L/H (blue)

Fig. 3. Bistable phenotype configurations. The left panel shows a surface plot of the sum of the partial densities which correspond to two metastable clusters. The ratio between x_1, x_2 defines the phenotypes. In (a) we see high activation levels in both x_1 and x_2, and thus can classify a High/High (H/H) phenotype. High activation in x_1 and low activation in x_2, describes a H/L phenotype. Similarly, we see bistable clusters of phenotypes in (c) H/L and L/H, in (e) L/L and H/L and in (g) L/L and L/H. The right panel shows calculated transition path flow directions in (b), (d), (f) and (h). In these transition flow graphs, the red colored set indicates the starting set and the blue colored set the ending set. The gray colored area represents the transition flow. The Table A.5 gives a quantitative overview over the transition dynamics, including the respective paths and probabilities.

changes in case 1 when we vary the conversion factor. When the factor decreases, the two density peaks move towards smaller copy numbers. The H/H peak becomes smaller compared to the H/L peak, until the two peaks merge into one and bistability is lost. In the other direction, increasing V moves the two peaks towards higher copy numbers, thereby increasing the statistical weight of the H/H peak and decreasing the H/L peak. The larger the conversion factor, the less probable the H/L state becomes, and stochastic transitions get more and more rare. Similar observations can be made for the other parameter sets.

4. Discussion

Informed knowledge about phenotype states, paths and their probabilities in a realistic setting is crucial to predict the role and functionality of macrophage cells in disease progression and to better understand the underlying mechanisms. Until now, however, it was unclear how macrophages *behave* in their stochastic environment. Therefore, we designed a methodological approach to mimic the macrophage switching dynamics in a stochastic cellular environment.

A similar approach (to the one we present here) has been applied in Li et al. (2021) to other cell-fate decisions. However, there are several computational differences: (i) In Li et al. (2021), MSM is based

(a) Case 5, Subcase 3: Transition (grey) from L/L (red) to L/H (blue) over H/L (grey)

(b) Case 5, Subcase 3: Probabilities between L/L (red) and L/H (blue) over the H/L (grey) phenotype

(c) Case 5, Subcase 4: Transition (grey) from L/L (red) to H/L (blue) over L/H (grey)

(d) Case 5, Subcase 4: Probabilities between L/L (red) and H/L (blue) over the L/H (grey) phenotype

(e) Case 5, Subcase 5: Transition (grey) from L/H (red) to H/L (blue) over L/L (grey)

(f) Case 5, Subcase 5: Probabilities between L/H (red) and H/L (blue) over the L/L (grey) phenotype

(g) Case 5, Subcase 6: Transition (grey) from H/L (red) to L/H (blue) over L/L (grey)

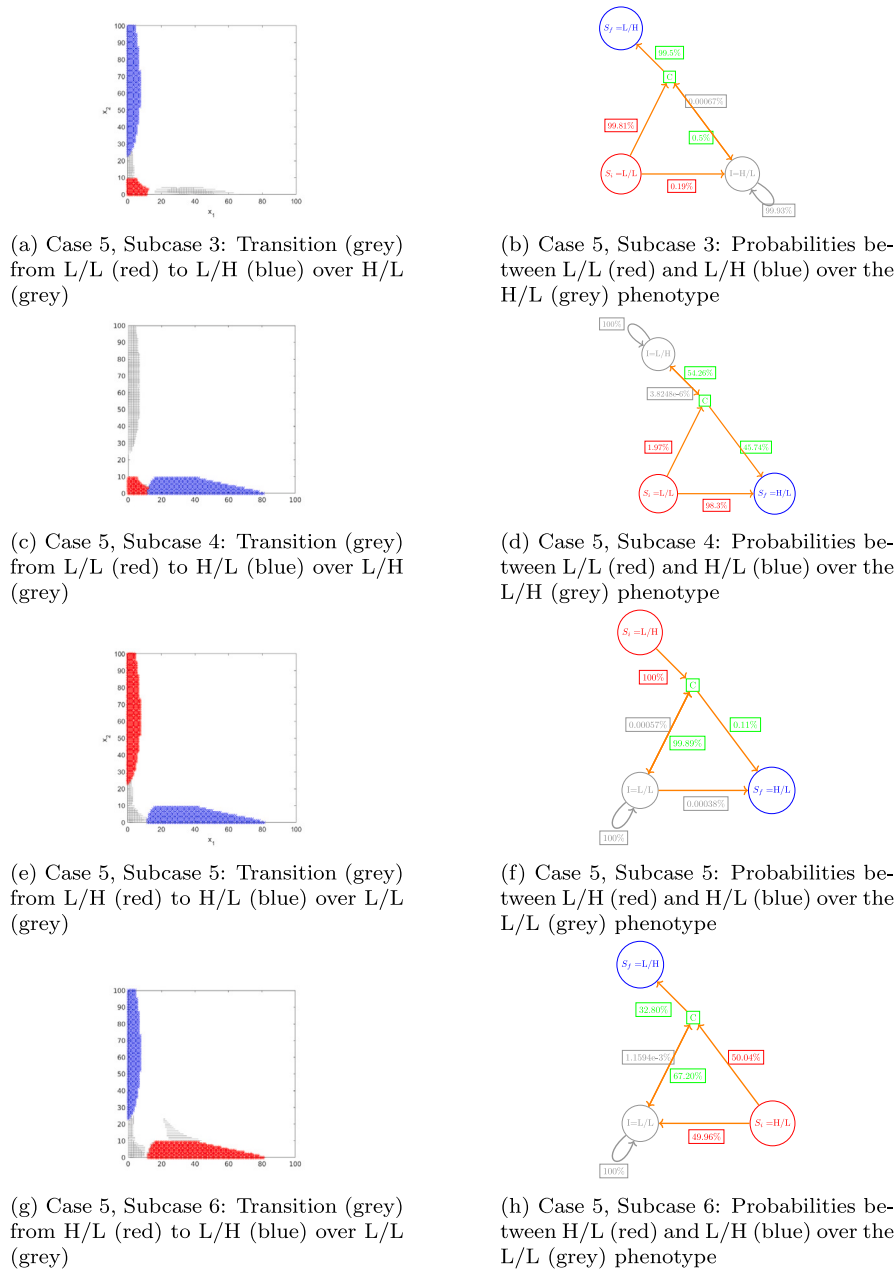(h) Case 5, Subcase 6: Probabilities between H/L (red) and L/H (blue) over the L/L (grey) phenotype

Fig. 4. Transition flows, paths and probabilities between three phenotypes. The left column shows transition path flow (in gray color) in the CME state-space between a given start phenotype (in red color) and end phenotype (in blue color). The right column presents the transition network together with the corresponding path segment probabilities, added next to the arrows of the flow direction. Red colored circles represent the start sets (S_i, with i for initial), and blue ones the end sets (S_f, with f for final). Intermittent phenotype states (I) are colored in gray and green represents the state space without any phenotype, i.e., the complement set (C) to the states (S_i, I and S_f). The path probabilities were calculated from Eq. (6) in Section 2. Their color refers to the set from where the transition flow comes. Table A.6 gives a quantitative overview over the transition dynamics, including all possible transition paths and their respective probabilities. Sub-cases 1 and 2 with combined end and start states are presented in Fig. A.8.
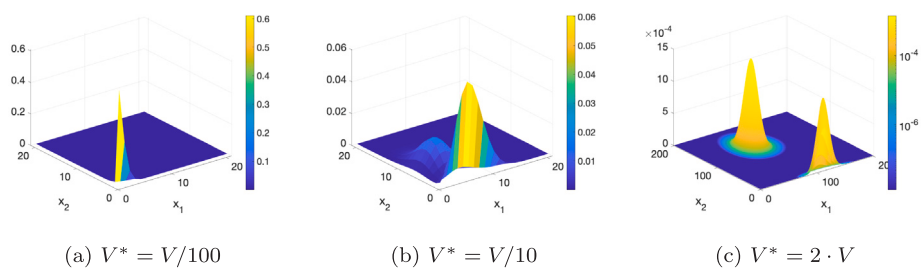

(a) $V^* = V/100$

(b) $V^* = V/10$

(c) $V^* = 2 \cdot V$

Fig. 5. Stationary density from simulations of case 1 with varying conversion factor V^*. The value of the original conversion factor is $V = 12.9$.

on simulation counts from the SSA to define the transition matrix. We define the transition rate matrix directly using the birth- and death-terms from a deterministic ODE model described in Frank et al. (2021). Hence, our approach is not restricted by simulation length. (ii) As in Li et al. (2021), we applied a PCCA type algorithm to partition the state space into fewer metastable states. The algorithm, as described in Frank et al. (2022), was extended to also deal with irreversible Markov chains, which makes it applicable to a wider range of biological processes. (iii) Instead of applying TPT on all micro-states as in Li et al. (2021), we adapted a coarse-grained version of TPT only between the identified phenotypes, which is less computational intensive.

Gene regulatory networks underlying macrophage polarization are exceedingly complicated (Wang et al., 2014). There have been many approaches to represent them using complex models, e.g., Palma et al. (2018), Zhao et al. (2019), Hörhold et al. (2020), Castiglione et al. (2016), Mishra et al. (2021), in the attempt to cover more molecular details and to couple them to large, non-linear and high-dimensional data sets.

On the contrary, we have employed a *parsimonious*, phenomeno-logical model of the macrophage polarization process with the aim to increase interpretability of our results and gain interesting bio-logical insights. Our simple model also avoids unnecessary and com-plex assumptions about possible relationships and connections between transcription factors and is therefore more easily generalizable and applicable to other processes. With fewer number of unknown model parameters, our model will be less prone to overfitting when coupled with (sparse) experimental data; it requires less computations and memory storage and is consequentially computationally more efficient.

We have shown that phenotype multistability is maintained in the stochastic setting, but that the number and combinations of emerging phenotypes differ from a deterministic approach, as compared to the results in Frank et al. (2021). This illustrates the influence and sensitiv-ity of single-cell decisions to random fluctuations, which is in line with prior work by Chu et al. (2017), Tse et al. (2018), Gupta et al. (2011), where the authors analyzed how stochasticity affects cell-fate-decisions of cancer, embryonic stem cells or closed gene regulatory network motifs. In addition, we gained first insights into the probabilistic nature of macrophage phenotype switches, which depends on the number of phenotypes, the specific type, as well as the switch direction.

In particular, our analysis revealed that for different parameter configurations, different phenotypes (e.g., L/L, H/L, L/H and H/H) emerge. These phenotypes coincide with those identified in Frank et al. (2021). However, our results also indicate that the number of multistable phenotypes (e.g., quadstable) in stochastic systems is restricted to bi- and at most tristability, which is in accordance with the current literature (Gupta et al., 2011; Geiß et al., 2011; Cas-tiglione et al., 2016). The validity of this hypothesis would have a huge impact on our understanding of macrophage cells and needs to be confirmed. Furthermore, the biological mechanisms behind changes in different phenotype configurations need more attention, especially as macrophage polarization is dynamic across time (Murray, 2017). For example, our observation that specific parametric sets leading to different phenotype outcomes can evolve from one another or in some cases remain mutually exclusive should be replicated in laboratory experiments, and their kinetic parameters within the cells should be quantified. Such an endeavor is a crucial first step to actually reconcile the biologically observed macrophage phenotypes and computational results (Eftimie and Barelle, 2021; Tse et al., 2018). The overall lack of data on macrophage markers restricts our knowledge about corre-sponding kinetic parameters and consequently on macrophage subtypes and their transition behavior (Eftimie and Barelle, 2021). The authors in, e.g., Zhao et al. (2019) have used experimental data on activated transcription factors from Western blot analyses to validate their model. The data show short activation profiles over time, but do not reflect multistable events. This restricts also our analysis and results to purely

synthetic scenarios and warrants the need for more data on macrophage phenotype subtypes, their markers and kinetic parameters to gain better understanding of the underlying processes of these heterogeneous cells through modeling in the future. In the following, our findings are therefore validated against empirical evidence for multistability of macrophages and state switches existing in the current literature.

Considering the level of activation of STAT1 and STAT6, we could interpret the L/H phenotype as M2-like, and H/L phenotype as M1-like, while H/H would represent a mixed phenotype and L/L an M0 phenotype (Frank et al., 2021). While the M0, M1 and M2 phenotypes are known to exist, mixed phenotypes (i.e., H/H) are less common. Indeed, unique or mixed phenotypes have been observed (Sica and Mantovani, 2012), particularly in pathological contexts such as neu-rodegenerative disorders (Garofalo et al., 2003) or the tumor mi-croenvironment (Biswas et al., 2008). For example, mixed phenotype macrophages have been recently observed in early-stage lung can-cer (Singhal et al., 2019) as well as human breast cancer (Deligne et al., 2020) and there are open questions both about the biological mechanisms which lead to their existence and their importance in tumor progression and control (Eftimie and Barelle, 2021).

Recent biological experiments in phenotype profiling (Singhal et al., 2019) have also demonstrated that tumor associated macrophages (TAMs) in early lung cancer often demonstrate a mixed phenotype, coexpressing M1 and M2 markers. This result indicates that in early-stage tumors, the phenotype of macrophages is mixed and not skewed towards either M1 or M2. It is well known that in advanced tumors, M2 macrophages are abundant (Yang et al., 2020), indicating that a large population of macrophages undergo a phenotype switch (or switches) as the tumor progresses. Similar observations have been made in Malyshev and Malyshev (2015). Here the authors describe a "switch phenotype" or "M3-phenotype", which actually mixes attributes from both the M1 and M2 phenotypes and has been observed in experiments when the phenotype spectrum shifted from M1 to M2 or vice versa. In our results, we have observed such a shift between the M1 to the M2 phenotypes over the complement set, which implies that the phenoytpe has to mix M1 and M2 attributes temporarily to reach the other "side". The hypotheses made by Malyshev and Malyshev (2015), however, indicate that another path exists that leads through a stable fourth phenotype, similar to the H/H one observed in the bistable situation, linking M1 and M2. Although our results did not confirm their claim, we cannot rule out the existence of such a phenotype and transition path.

In addition, our results show that bistable phenotype switches are faster than switches between three phenotypes. This result coincides with the finding in Eftimie and Barelle (2021) that macrophage phe-notypes have different half-life spans (e.g., M1 and mixed phenotypes have shorter spans), which consequently could impact the speed of specific transitions. If, for example, a transition path passes through an intermediate phenotype that has a long half-life, the switch to the end phenotype would take longer time. In our results, such an observation was specifically clear in the M1–M2 phenotype transition over the M0 state, which led to very long average transition duration. This duration reflects the energy barrier that has to be crossed for the phenotypes to switch states (Kim and Wang, 2007). For example, the longer the time, the more energy is needed for a transition and the robuster are the phenotype states (Kim and Wang, 2007). A similar observation has also been confirmed in a study on cancer cells, where the authors showed that specific phenotype configurations were maintained over a long time period (Gupta et al., 2011).

Finally, the transition network probabilities in Gupta et al. (2011) for cancer sub-populations are comparable in terms of rate and magni-tude to our results in the tristable case. In particular, the study shows that some phenotypes have a very high probability to remain in a specific state once this state has been reached. The observation that

cancer stem like cells arise form non-stem-like cells, is similar to our observation of the L/L (M0-like) phenotype (Gupta et al., 2011). Although cancer and macrophage cells are not identical, they share similar attributes like heterogeneity and plasticity (Yabo et al., 2022). Thus, the observed similarities, between our study and the results by Gupta et al. (2011), in transition dynamics might be another common attribute of these cell types. This inference however needs further investigation. In addition, future studies should investigate if the transition probabilities for single macrophage cells coincide with data from in-vivo and in-vitro experiments and how these probabilities are altered in populations of macrophage cells. Particularly, the presented methodological approach in this manuscript could be of use for such future work.

Intermediate states have also been observed in embryogenesis during the epithelial-mesenchymal transition, which is critical for organ and tissue development (Lang et al., 2021) and also plays a role in cancer metastasis (Goetz et al., 2020). Intermediate states were found to accelerate the epithelial-mesenchymal transition because cells can make small changes on gene expression as a first step towards a transition, but remain in the intermediate state due to its level of stability (Lang et al., 2021). The authors suggest that the presence of intermediate states increases the plasticity of cell fate transitions. It is becoming apparent that many cellular processes have multiple intermediate states rather than just a binary outcome, and the role of these states may be to maintain plasticity. In the context of macrophage polarization, this is desirable as macrophages must be plastic to respond to their changing environment (Shapouri-Moghaddam et al., 2018).

Overall, we have shown that our methodological approach is a useful tool to uncover the underlying dynamic differences in multistable systems and to test different hypotheses about potential configuration states. This paradigm could be applied beyond macrophage polarization, and an advantage of this framework is the simple construction of the model. Many cell fate decisions are controlled by pairs of antagonistic master regulators (Zhou and Huang, 2011) which can be represented by small networks with mutual inhibition and self-stimulation. Examples include Cdx2 and Oct4 in the embryo (Ralston and Rossant, 2005) and Nkx6 and Ptf1a, in the pancreas (Schaffer et al., 2010). Thus our approach can potentially be applied to a wide range of paired cell-fate decisions.

Although we studied a rather simple system with two transcription factors and two input signals, the simplicity of our approach allows to easily expand on the number of those to study specific components of macrophage polarization related to particular diseases (Dorrington and Fraser, 2019). In addition, further exploration of the parameter space using, e.g., Latin Hypercube Sampling (Stein, 1987; McKay et al., 2000), could lead to a broader range of parameters for multistability, and therewith reveal different dynamics. Such an analysis however exceeds the scope of this study.

Upon the availability of more data on macrophages and their kinetic parameters, we believe that this approach will be of great importance to further investigate and clarify our understanding of the mechanisms behind particular cell transition pathways. Single-cell RNA-seq can reveal immune heterogeneity by revealing a large number of genes per cell and makes it possible to identify previously unknown macrophages subsets. For example, Dick et al. (2019) recently identified a new set of macrophages whose population increases after cardiac injury. More evidence of mixed phenotype macrophages will undoubtedly unfold.

CRediT authorship contribution statement

Anna-Simone Josefine Frank: Conceptualization, Methodology, Software, Validation, Formal analysis, Investigation, Writing – original draft, Writing – review & editing, Visualization. **Kamila Larripa:** Conceptualization, Methodology, Validation, Formal analysis, Investigation, Writing – original draft, Writing – review & editing, Visualization, Funding acquisition. **Hwayeon Ryu:** Conceptualization, Methodology, Validation, Formal analysis, Investigation, Writing – original

draft, Writing – review & editing, Visualization, Funding acquisition. **Susanna Röblitz:** Conceptualization, Methodology, Software, Validation, Formal analysis, Investigation, Writing – original draft, Writing – review & editing, Visualization, Supervision, Funding acquisition.

Declaration of competing interest

The authors declare that they have no known competing financial interests or personal relationships that could have appeared to influence the work reported in this paper.

Data statement

This manuscript uses no biological or experimental data. All figures can be reproduced using the mathematical model, the parameters and numerical specifications presented in this manuscript. The Matlab code (macro-tpt Frank and Röblitz (2022)) for all presented cases is available on GitHub (https://github.com/a-sfrank/macro-tpt.git). The cPCCA+ Matlab code, as described in Frank et al. (2022), was downloaded from GitHub (https://github.com/sroeblitz/cPCCA.git), adapted and integrated into our implementation.

Appendix

A.1. Transition path theory

TPT takes as input the transition rate matrix $Q = (\ell_{ij})_{i,j \in S} = Q(i,j)_{i,j \in S}$ of a Markov jump process $\{X\}_{t \in \mathbb{R}}$ defined on a discrete state space S. Based on the assumption that the process $\{X\}_{t \in \mathbb{R}}$ is irreducible and ergodic, the time-reversed process $\{\tilde{X}\}_{t \in \mathbb{R}}$ is also a Markov jump process with a rate matrix $\tilde{Q} = (\tilde{\ell})_{i,j \in S}$ given by $\tilde{\ell}_{i,j} = \frac{\pi_j}{\pi_i} \ell_{ji}$ (Metzner et al., 2009), where π is the invariant distribution (or stationary density) of both processes $\{X\}_{t \in \mathbb{R}}$ and $\{\tilde{X}\}_{t \in \mathbb{R}}$.

TPT is based on *reactive trajectories*, which are defined as transitions between two non-empty, disjoint subsets A and B of the state-space S, where one set is the source and the other one is the sink state (Noé et al., 2009; Metzner et al., 2009).

The discrete forward q^+ and backward q^- committor functions are essential to calculate statistical properties and dynamical information of the reactive trajectories. The forward committor q^+ is defined by Metzner et al. (2009), as follows,

$$\begin{cases} \sum_{j \in S} \ell_{ij} q_j^+ = 0 & \forall i \in (A \cup B)^c \\ q_j^+ = 0 & \forall i \in A, \\ q_j^+ = 1 & \forall i \in B, \end{cases} \tag{A.1}$$

Table A.3

Nomenclature of Transition Path Theory (TPT). Table presents the dynamical information about the ensemble of reactive trajectories and their interpretations. Details on TPT can be found in Section 2 and Appendix.

| Symbol	Name	Interpretation
Entire state space		
$A \rightarrow B$	Reactive trajectory from A to B	A trajectory that leaves A and enters B without returning to A in between
q^+	Forward committor	Prob. that a trajectory initiated in A will reach B before A
q^-	Backward committor	Prob. that a trajectory initiated in B will reach A before B
f_{ij}^{AB}	Prob. current of reactive trajectories	Average rate at which a reactive trajectory from A to B transitions from state i to state j
f_{AB}^+	Effective current	$f_{ij}^+ = \max(f_{ij}^{AB} - f_{ji}^{AB}, 0)$
μ_i^{AB}	Prob. distribution of reactive trajectories	Prob. that a reactive trajectory passes through state i
t_{AB}	Transition time	Average time duration of a transition from A to B
$k^{A\rightarrow}$	Transition rate out of A	Average rate at which trajectories leave A
$k^{\rightarrow B}$	Transition rate into B	Average rate at which trajectories enter B
CG state space		
$\tilde{\pi}_S$	Total stationary prob. of macrostate S	
$\tilde{F}_{S_i \rightarrow S_f}$	Coarse-grained flux between macrostates S_i and S_f	
$\tilde{T}_{S_i \rightarrow S_f}$	Transition probability between macrostates S_i and S_f	Inter-macrostate transitions (based on source-state S_i)
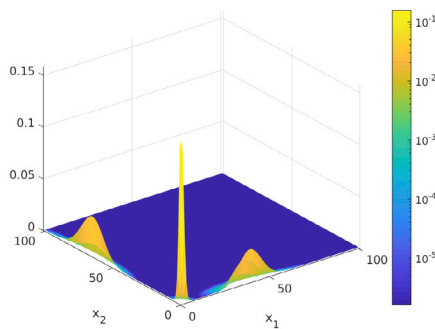
Fig. A.6. Three macrophage phenotypes: Surface plot of the sum of the three partial densities corresponding to the three identified metastable clusters. The ratio between x_1, x_2 characterize the phenotype: Low activation in x_1 and high activation level in x_2 describes the Low/High (L/H) phenotype. Low activation in x_1 and low activation level in x_2 describes the Low/Low (L/L) phenotype, and high activation in x_1 and low activation level in x_2 describes the High/Low (H/L) phenotype.

and the backward committor q^- as

$$\begin{cases} \sum_{j \in S} \tilde{\ell}_{ij} q_j^- = 0 & \forall i \in (A \cup B)^c \\ q_j^- = 1 & \forall i \in A, \\ q_j^- = 0 & \forall i \in B. \end{cases} \tag{A.2}$$

Given the above definitions of committor functions, rate matrices and stationary densities, we can calculate statistical properties that allow for a dynamical interpretation of the ensemble of reactive trajectories between subsets A and B in the state space S (Helfmann et al., 2020). Table A.3 summarizes important measures in TPT to describe dynamical information and states the corresponding interpretation.

For any $i \in S$, the *distribution of reactive trajectories* $\mu^R = (\mu_i^R)_{i \in S}$ is given by (see Metzner et al. (2009))

$$\mu_i^R = \pi_i q_i^+ q_i^-. \tag{A.3}$$

Normalizing μ_i^R by *the probability to be on a transition at time t* (i.e., $Z_{AB} = \sum_{j \in S} \pi_j q_j^+ q_j^-$) (Helfmann et al., 2020), one defines the *normalized distribution of reactive trajectories* (μ_i^{AB}) (Metzner et al., 2009), as

$$\mu_i^{AB} = Z_{AB}^{-1} \mu_i^R. \tag{A.4}$$

Two other important statistics are the *net average number of reactive trajectories observed per time unit* (f_{ij}^+) and the *average number of transitions from A to B per time unit* (k_{AB}) (Metzner et al., 2009).

The definitions of f_{ij}^+ and k_{AB} build on the *probability current of reactive trajectories*, f_{ij}^{AB}, which is defined in Metzner et al. (2009) as follows: For all pairs of states $(i, j), i, j \in S, i \neq j$,

$$f_{ij}^{AB} = \pi_i q_i^- \ell_{ij} q_j^+, \quad \text{where } \ell_{ij} = Q(i, j). \tag{A.5}$$

f_{ij}^{AB} describes the average rate at which a reaction trajectory transitions from state i to state j. Moreover, the *transition rate* from A to B, k_{AB}, is given by

$$k^{AB} = \underbrace{\sum_{i \in A, j \in S} f_{ij}^{AB}}_{k^{A\rightarrow}} = \underbrace{\sum_{i \in S, j \in B} f_{ij}^{AB}}_{k^{\rightarrow B}}, \tag{A.6}$$

where $k^{A\rightarrow}$ and $k^{\rightarrow B}$ are the discrete rates of leaving A and entering B, respectively (see Metzner et al. (2009), Helfmann et al. (2020)). Equality in Eq. (A.6) holds for stationary Markov processes $\{X_t\}_{t \in \mathbb{R}}$ (Helfmann et al., 2020). The *effective current* f_{ij}^+ is defined by (see Metzner et al. (2009))

$$f_{ij}^+ = \max(f_{ij}^{AB} - f_{ji}^{AB}, 0). \tag{A.7}$$

Furthermore, the *average time duration of a transition from A to B*, t^{AB}, is defined in Helfmann et al. (2020) by

$$t^{AB} := \frac{Z^{AB}}{k^{AB}}. \tag{A.8}$$

While the above characteristics are defined on the entire state space S, we consider for the following definitions the coarse-grained sets from the Markov State Model, which is defined by matrix $P_c(\tau)$. For the coarse partition of the state space $\tilde{S} = \{S_1, \ldots, S_n\}$, where A and B
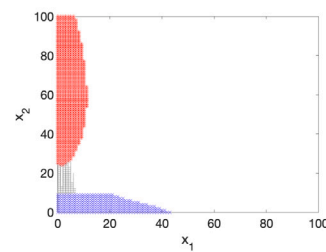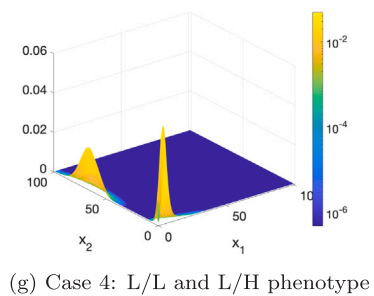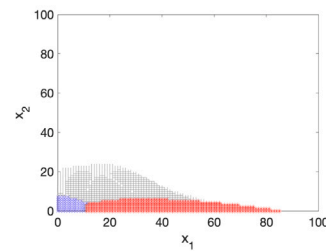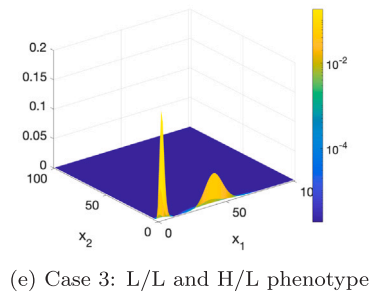
(a) Case 1: H/H and H/L phenotype

(b) Case 1: Transitions (grey) from H/L (red) to H/H (blue)

(c) Case 2: H/L and L/H phenotype

(d) Case 2: Transitions (grey) from L/H (red) to H/L (blue)

(e) Case 3: L/L and H/L phenotype

(f) Case 3: Transitions (grey) from H/L (red) to L/L (blue)

(g) Case 4: L/L and L/H phenotype

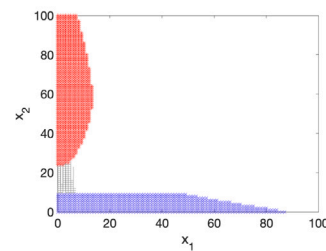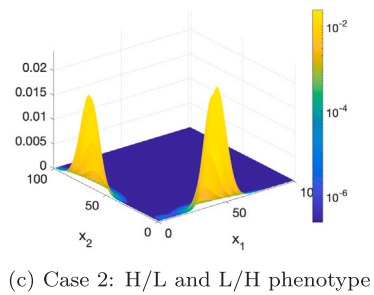(h) Case 4: Transitions (grey) from L/H (red) to L/L (blue)
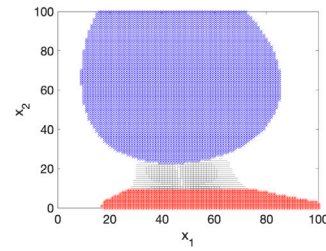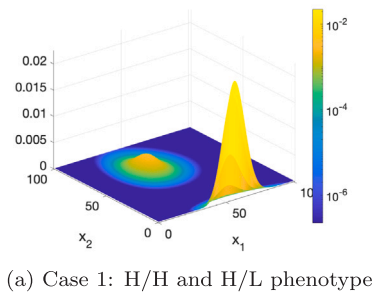
Fig. A.7. Bistable phenotype configurations. The left panel shows a surface plot of the sum of the partial densities which correspond to two metastable clusters. The ratio between x_1, x_2 defines the phenotypes. In (a) we see high activation levels in both x_1 and x_2, and thus can classify a High/High (H/H) phenotype. High activation in x_1 and low activation in x_2, describes a H/L phenotype. Similarly, we see bistable clusters of phenotypes in (c) H/L and L/L, in (e) L/L and H/L, and in (g) L/L and L/H. The right panel shows calculated transition path flow directions in (b), (d), (f) and (h). The red colored set indicates the starting set, blue the ending set and gray the transition flow.

Table A.4

Clustering results from PCCA+. Table shows the number of metastable states (i.e., phenotypes), the calculated eigenvalues ($\lambda_i, i = \{1, 2, 3, 4\}$) and gaps, cluster weights ($\omega_i, i = \{1, 2\}$), transition rate matrix Q_c, and transition probability matrix P_c for the respective five parameter sets ("Case").

Case	# phenotypes	Eigenval. of Q_c	Cluster weights	Transition state matrix	Transition prob. matrix
1	2	$\lambda_1 = 0$ $\lambda_2 = -0.9884$ $(\lambda_3 = -0.9997)$	$\omega_1 = 0.10031$ $\omega_2 = 0.89969$	$Q_c = 10^{-4} \cdot \begin{pmatrix} 0.4707 & -0.4707 \\ -0.6109 & 0.6109 \end{pmatrix}$	$P_c = \begin{pmatrix} 0.9981 & 0.0019 \\ 0.0000 & 1.0000 \end{pmatrix}$
2	2	$\lambda_1 = 1.000$ $\lambda_2 = 0.9962$ $(\lambda_3 = 0.0008)$	$\omega_1 = 0.099103$ $\omega_2 = 0.9009$	$Q_c = 10^{-4} \cdot \begin{pmatrix} -0.3860 & 0.3860 \\ 0.0625 & -0.0625 \end{pmatrix}$	$P_c = \begin{pmatrix} 0.9962 & 0.0038 \\ 0.0000 & 1.0000 \end{pmatrix}$
3	2	$\lambda_1 = 0$ $\lambda_2 = -0.0214$ $(\lambda_3 = -4.6872)$	$\omega_1 = 0.45748$ $\omega_2 = 0.54252$	$Q_c = \begin{pmatrix} -0.0269 & 0.0269 \\ 0.0272 & -0.0272 \end{pmatrix}$	$P_c = \begin{pmatrix} 0.1243 & 0.8757 \\ 0.0068 & 0.9932 \end{pmatrix}$
4	2	$\lambda_1 = 0$ $\lambda_2 = -0.0021$ $(\lambda_3 = -0.9261)$	$\omega_1 = 0.097708$ $\omega_2 = 0.90229$	$Q_c = \begin{pmatrix} -0.0024 & 0.0024 \\ 0.0001 & -0.0001 \end{pmatrix}$	$P_c = \begin{pmatrix} 0.8094 & 0.1906 \\ 0.0001 & 0.9999 \end{pmatrix}$
5	3	$\lambda_1 = 0,$ $\lambda_2 = -2.8653 \cdot 10^{-5}$ $\lambda_3 = -6.1945 \cdot 10^{-4}$ $(\lambda_4 = -0.9902)$	$\omega_1 = 0.016006$ $\omega_2 = 0.084884$ $\omega_3 = 0.89911$	$Q_c = 10^{-3} \cdot \begin{pmatrix} -0.0327 & 0.0033 & 0.0294 \\ 0.6020 & -0.6075 & 0.0055 \\ -0.0042 & 0.0043 & -0.0001 \end{pmatrix}$	$P_c = \begin{pmatrix} 0.9957 & 0.0014 & 0.0029 \\ 0.0580 & 0.9414 & 0.0006 \\ 0.0000 & 0.0000 & 1.0000 \end{pmatrix}$

Table A.5

Transition Path Theory (TPT) results for sets of two phenotype states (two each of L/L, H/L, L/H, H/H). Each subcase specifies the start and end sets of the transition directions, as well as complement (C) set, as well as the average time duration (t) it takes for a phenotype to switch. Based on the coarse-grained transition fluxes between metastable (phenotype) sets (e.g., S_i indicates the initial set and S_f the final set), all possible transition paths and their probabilities are calculated as described in Section 2. See Table A.3 for description and interpretation of TPT nomenclature. Methodological details are presented in Section 2 and in Appendix.

	Case 1: Forward		Case 1: Backward		Case 2: Forward		Case 2: Backward
Start:	H/L	Start:	H/H	Start:	L/H	Start:	H/L
End:	H/H	End:	H/L	End:	H/L	End:	L/H

Statistics: Average time duration per transition

t	3.508329e−01	t	1.888526e−01	t	1.745843e−01	t	5.180507e−01

Coarse-grained flux directions and amount:

$S_i \to S_f$	$\tilde{F}_{S_i \to S_f}$	$S_i \to S_f$	$\tilde{F}_{S_i \to S_f}$	$S_i \to S_f$	$\tilde{F}_{S_i \to S_f}$	$S_i \to S_f$	$\tilde{F}_{S_i \to S_f}$
$H/L \to H/H$	0	$H/H \to H/L$	0	$L/H \to H/L$	0	$H/L \to L/H$	0
$H/L \to C$	4.030848e−14	$H/H \to C$	7.307069e−14	$L/H \to C$	2.126413e−14	$H/L \to C$	1.236879e−14
$H/H \to H/L$	0	$H/L \to H/H$	0	$H/L \to L/H$	0	$L/H \to H/L$	0
$H/H \to C$	0	$H/L \to C$	0	$H/L \to C$	0	$L/H \to C$	0
$C \to H/L$	0	$C \to H/H$	0	$C \to L/H$	0	$C \to H/L$	0
$C \to H/H$	1.404820e−14	$C \to H/L$	2.257171e−14	$C \to H/L$	7.004957e−15	$C \to L/H$	3.946240e−15

Transition paths and transition probabilities

$S_i \to S_f$		$S_i \to S_f$		$S_i \to S_f$		$S_i \to S_f$	
$H/L \to H/H$	0%	$H/H \to H/L$	0%	$L/H \to H/L$	0%	$H/L \to L/H$	0%
$H/L \to C \to H/H$	100%	$H/H \to C \to H/L$	100%	$L/H \to C \to H/L$	100%.	$H/L \to C \to L/H$	100%

	Case 3: Forward		Case 3: Backward		Case 4: Forward		Case 4: Backward
Start:	L/L	Start:	H/L	Start:	L/L	Start:	L/H
End:	H/L	End:	L/L	End:	L/H	End:	L/L

Statistics: Average time duration per transition

t	1.776616e−07	t	1.395691e−06	t	4.367060e−01	t	1.784335e−01

Coarse-grained flux directions and amount:

$S_i \to S_f$	$\tilde{F}_{S_i \to S_f}$	$S_i \to S_f$	$\tilde{F}_{S_i \to S_f}$	$S_i \to S_f$	$\tilde{F}_{S_i \to S_f}$	$S_i \to S_f$	$\tilde{F}_{S_i \to S_f}$
$L/L \to H/L$	1.232997e−04	$L/L \to H/L$	0	$L/L \to L/H$	0	$L/L \to L/H$	0
$L/L \to C$	5.619505e−09	$L/L \to C$	0	$L/L \to C$	1.009425e−14	$L/L \to C$	0
$H/L \to L/L$	0	$H/L \to L/L$	9.039354e−05	$L/H \to L/L$	0	$L/H \to L/L$	0
$H/L \to C$	0	$H/L \to C$	2.660313−08	$L/H \to C$	0	$L/H \to C$	2.052825e−14
$C \to L/L$	0	$C \to L/L$	4.933935e−10	$C \to L/L$	0	$C \to L/L$	6.876109e−15
$C \to H/L$	7.050022e−11	$C \to H/L$	0	$C \to L/H$	3.554568e−15	$C \to L/H$	0

Transition paths and transition probabilities:

$S_i \to S_f$		$S_i \to S_f$		$S_i \to S_f$		$S_i \to S_f$	
$L/L \to H/L$	99.99%	$H/L \to L/L$	99.97%	$L/L \to L/H$	0%	$L/H \to LL$	0%
$L/L \to C \to H/L$	0.01%	$H/L \to C \to L/L$	.03%	$L/L \to C \to L/H$	100%	$L/H \to C \to LL$	100%

Table A.6

Transition Path Theory (TPT) results for three phenotype states (L/L, H/L and L/H). Each subcase specifies the start and end sets of the transition directions, as well as intermittent (I) or complement (C) set, as well as the average time duration (t) it takes for a phenotype to switch. Based on the coarse-grained transition fluxes between metastable (phenotype) sets (e.g., S_i indicates the initial set and S_f the final set), all possible transition paths and their probabilities are calculated as described in Section 2. See Table A.3 for description and interpretation of TPT nomenclature. Methodological details are presented in Section 2 and in Appendix. Abbreviations: "Compl." refers to the complement set (C); "Inter." stands for intermittent set (I).

Subcase 1		Subcase 2		Subcase 3	
Start:	L/L	Start:	L/L & H/L	Start:	L/L
End:	L/H & H/L	End:	L/H	End:	L/H
Compl.:	C	Compl.:	C	Compl.:	C
Inter.:	–	Inter.:	–	Inter.:	H/L
Statistics: Average time duration per transition					
t	1.645091e−01	t	4.010152e−01	t	2.031077e+00
Coarse-grained flux directions and amount:					
$S_i \rightarrow S_f$	$\tilde{F}_{S_i \rightarrow S_f}$	$S_i \rightarrow S_f$	$\tilde{F}_{S_i \rightarrow S_f}$	$S_i \rightarrow S_f$	$\tilde{F}_{S_i \rightarrow S_f}$
$L/L \rightarrow H/L$	4.283462e−14	$L/L \rightarrow C$	3.6797e−14	$L/L \rightarrow H/L$	6.947925e−17
$L/L \rightarrow C$	3.765562e−14	$H/L \rightarrow C$	3.913517e−15	$L/L \rightarrow C$	3.679917e−14
$C \rightarrow H/L$	7.501706e−16	$C \rightarrow L/H$	1.136061e−14	$H/L \rightarrow H/L$	2.360166e−11
$C \rightarrow L/H$	1.049604e−14			$H/L \rightarrow C$	1.576060e−16
				$C \rightarrow L/H$	1.051028e−14
				$C \rightarrow H/L$	5.286661e−17
Transition paths and transition probabilities					
$L/L \rightarrow C \rightarrow L/H$	43.66%	$L/L \rightarrow C \rightarrow L/H$	90.39%	$L/L \rightarrow C \rightarrow L/H$	99.31%
$L/L \rightarrow H/L$	53.22%	$H/L \rightarrow C \rightarrow L/H$	9.61%	$L/L \rightarrow H/L \rightarrow C \rightarrow L/H$	1.2615e−6%
$L/L \rightarrow C \rightarrow H/L$	3.12%			$L/L \rightarrow C \rightarrow H/L \rightarrow C \rightarrow L/H$	3.3135e−6%

Subcase 4		Subcase 5		Subcase 6	
Start:	L/L	Start:	L/H	Start:	H/L
End:	H/L	End:	H/L	End:	L/H
Compl.:	C	Compl.:	C	Compl.:	C
Inter.:	L/H	Inter.:	L/L	Inter.:	L/L
Statistics: Average time duration per transition					
t	1.353744e+05	t	6.990304e+03	t	1.359403e+04
Coarse-grained flux directions and amount:					
$S_i \rightarrow S_f$	$\tilde{F}_{S_i \rightarrow S_f}$	$S_i \rightarrow S_f$	$\tilde{F}_{S_i \rightarrow S_f}$	$S_i \rightarrow S_f$	$\tilde{F}_{S_i \rightarrow S_f}$
$L/L \rightarrow H/L$	4.292451e−14	$L/H \rightarrow C$	2.185682e−14	$H/L \rightarrow L/L$	5.811830e−15
$L/L \rightarrow C$	8.647682e−16	$L/L \rightarrow H/L$	8.438635e−15	$H/L \rightarrow C$	5.821236e−15
$L/H \rightarrow C$	3.139963e−14	$L/L \rightarrow C$	1.250078e−14	$L/L \rightarrow C$	2.650196e−14
$L/H \rightarrow L/H$	8.209541e−07	$L/L \rightarrow L/L$	2.208563e−09	$L/L \rightarrow L/L$	2.285861e−09
$C \rightarrow H/L$	7.515452e−16	$C \rightarrow H/L$	1.421303e−17	$C \rightarrow L/H$	3.960937e−15
$C \rightarrow L/H$	8.916429e−16	$C \rightarrow L/L$	1.310601e−14	$C \rightarrow L/L$	8.115767e−15
Transition paths and transition probabilities:					
$L/L \rightarrow H/L$	98.30%	$L/H \rightarrow C \rightarrow H/L$	0.11%	$H/L \rightarrow C \rightarrow L/H$	16.41%
$L/L \rightarrow C \rightarrow H/L$	0.90%	$L/H \rightarrow C \rightarrow L/L \rightarrow C \rightarrow H/L$	6.2193e−7%	$H/L \rightarrow L/L \rightarrow C \rightarrow L/H$	1.8999e−4%
$L/L \rightarrow C \rightarrow L/H \rightarrow C \rightarrow H/L$	1.87e−8%	$L/H \rightarrow C \rightarrow L/L \rightarrow H/L$	3.8166e−4%	$H/L \rightarrow C \rightarrow L/L \rightarrow C \rightarrow L/H$	1.2783e−4%

are identical to individual S_i or a combination of several S_i, *the coarse-grained flux from set S_i to set S_f*, is defined, according to Noé et al. (2009), by

$$\tilde{F}_{S_i \rightarrow S_f} = \sum_{k \in S_i, l \in S_f} f_{k,l}^{AB} \tag{A.9}$$

Given the coarse-grained flux $\tilde{F}_{S_i \rightarrow S_f}$, we can now define *individual pathways P_i* connecting A and B (Noé et al., 2009), by connecting neighboring sets $S_i, i \in [n]$, with $S_1 = A$ and $S_n := B$, such that $\tilde{F}_{S_i \rightarrow S_f} \neq 0$.

Given the set of all individual pathways P_i from A to B, we describes the *relative probability* of a path segment from S_i to S_f (similar to Noé et al. (2009)) by

$$p_{S_i \rightarrow S_f}^r = \frac{\tilde{F}_{S_i \rightarrow S_f}}{\sum_{i = S_i, f \neq S_i} \tilde{F}_{S_i \rightarrow S_f}}, \tag{A.10}$$

where the sum represent the total flow from state S_i to neighboring states $S_j, j \in [n], j \neq i$ on the $A \rightarrow B$ transition paths.

Finally, the relative probabilities of the path segments $p_{S_i \rightarrow S_f}^r$ along an individual pathway P_i from A to B are combined to define the *total relative probability p_i^r of path P_i*.

Alternatively, there exist several, so called, *Path Decomposition Algorithms* (Metzner et al., 2009; Noé et al., 2009) that allow the decomposition into individual pathways P_i. However, if used on the entire state space S they can be computationally very expensive. Due to our relative small coarse-grained state space $\tilde{S}$, we decided to calculate the decomposition manually, as described above.

A.2. Tables
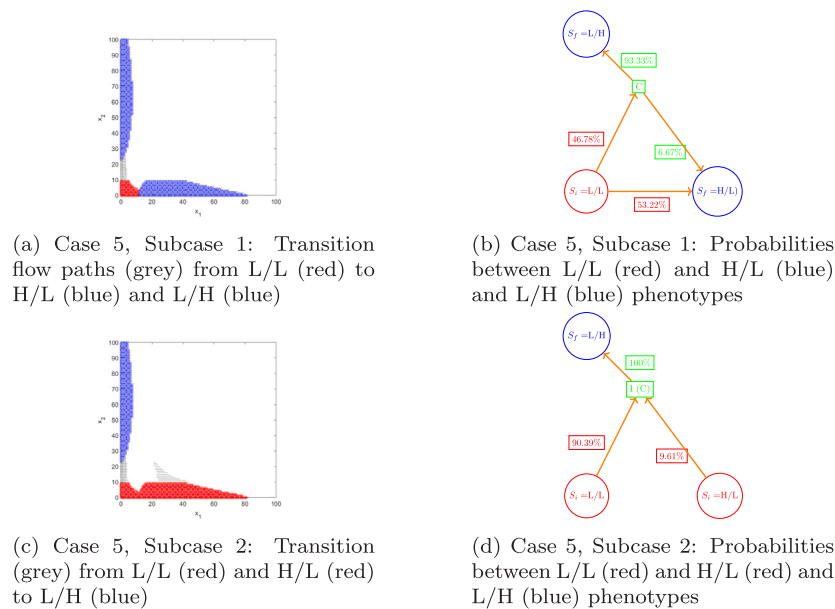
See Tables A.3–A.6.

A.3. Figures

See Figs. A.6–A.8

(a) Case 5, Subcase 1: Transition flow paths (grey) from L/L (red) to H/L (blue) and L/H (blue)

(b) Case 5, Subcase 1: Probabilities between L/L (red) and H/L (blue) and L/H (blue) phenotypes

(c) Case 5, Subcase 2: Transition (grey) from L/L (red) and H/L (red) to L/H (blue)

(d) Case 5, Subcase 2: Probabilities between L/L (red) and H/L (red) and L/H (blue) phenotypes

Fig. A.8. Transition flows, paths and probabilities between three phenotypes with combined start and end sets. The left column shows the transition path flow (in gray color) in the CME state-space between a given start set (in red color) and end set (in blue color). The right column represents the transition path flows in a transition network together with the corresponding path segment probabilities, which are added next to the arrows of the flow direction. Red colored circles represent the start sets (S_i, with i for initial), and blue ones the end sets (S_f, with f for final). Green color refers to the state space without any phenotype, i.e., the complement set (C) to the states (S_i and S_f). The path segment probabilities were calculated from Eq. (3) in Section 2. Their color refers to the set from where the transition flow comes. Table A.6 gives a quantitative overview over the transition dynamics, including all possible transition paths and their respective probabilities. Subcases 3–6 are presented in Fig. 4 in the article.

References

Bardi, G., Smith, M., Ryu, H., Hood, J., 2018. Melanoma exosomes promote mixed M1 and M2 macrophage polarization. Cytokine 105 (1769), 63–72. http://dx.doi.org/10.1016/j.cyto.2018.02.002.

Biswas, S.K., Mantovani, A., 2010. Macrophage plasticity and interaction with lymphocyte subsets: cancer as a paradigm. Nat. Immunol. 11 (10), 889–896. http://dx.doi.org/10.1038/ni.1937.

Biswas, S., Sica, A., Lewis, C., 2008. Plasticity of macrophage function during tumor progression: regulation by distinct molecular mechanisms. J. Immunol. 180 (4), 2011–2017. http://dx.doi.org/10.4049/jimmunol.180.4.2011.

Castiglione, F., Tieri, P., Palma, A., Jarrah, A.S., 2016. Statistical ensemble of gene regulatory networks of macrophage differentiation. BMC Bioinform. 17 (Suppl 19), 506. http://dx.doi.org/10.1186/s12859-016-1363-4.

Chu, B., Margaret, J., Sato, R., Read, E., 2017. Markov state models of gene regulatory networks. BMC Syst. Biol. 11 (14), 1–17. http://dx.doi.org/10.1186/s12918-017-0394-4.

Coomer, M., Ham, L., Stumpf, M., 2022. Noise distorts the epigenetic landscape and shapes cell-fate decisions. Cell Syst. 13 (1), 83–102. http://dx.doi.org/10.1016/j.cels.2021.09.002.

Czimmerer, Z., Daniel, B., Horvath, A., Rückerl, D., Nagy, G., Kiss, M., Peloquin, M., Budai, M.M., Cuaranta-Monroy, I., Simandi, Z., et al., 2018. The transcription factor STAT6 mediates direct repression of inflammatory enhancers and limits activation of alternatively polarized macrophages. Immunity 48 (1), 75–90. http://dx.doi.org/10.1016/j.immuni.2017.12.010.

Deligne, C., Murdamoothoo, D., Gammage, A., Gschwandtner, M., Erne, W., Loustau, T., Marzeda, A., Carapito, R., Paul, N., Velazquez-Quesada, I., Mazzier, I., Sun, Z., Orend, G., Midwood, K., 2020. Matrix-targeting immunotherapy controls tumor growth and spread by switching macrophage phenotype targeting microenvironmental cues to switch TAM phenotype. Cancer Immunol. Res. 8 (3), 368–382. http://dx.doi.org/10.1158/2326-6066.CIR-19-0276.

Dick, S.A., Macklin, J.A., Nejat, S., Momen, A., Clemente-Casares, X., Althagafi, M.G., Chen, J., Kantores, C., Hosseinzadeh, S., Aronoff, L., et al., 2019. Self-renewing resident cardiac macrophages limit adverse remodeling following myocardial infarction. Nat. Immunol. 20 (1), 29–39. http://dx.doi.org/10.1038/s41590-018-0272-2.

Dorrington, M.G., Fraser, I.D., 2019. NF-κb signaling in macrophages: dynamics, crosstalk, and signal integration. Front. Immunol. 10, 705. http://dx.doi.org/10.3389/fimmu.2019.00705.

Eftimie, R., Barelle, C., 2021. Mathematical investigation of innate immune responses to lung cancer: The role of macrophages with mixed phenotypes. J. Theoret. Biol. 524 (110739), 110739. http://dx.doi.org/10.1016/j.jtbi.2021.110739.

Frank, A., Larripa, K., Ryu, H., Snodgrass, R., Röblitz, S., 2021. Bifurcation and sensitivity analysis reveal key drivers of multistability in a model of macrophage polarization. J. Theoret. Biol. 509, 110511. http://dx.doi.org/10.1016/j.jtbi.2020.110511.

Frank, A., Röblitz, S., 2022. a-sfrank/macro-tpt: v1.0.0. Zenodo, http://dx.doi.org/10.5281/zenodo.7243749.

Frank, A., Sikorski, A., Röblitz, S., 2022. Spectral clustering of Markov chain transition matrices with complex eigenvalues. http://dx.doi.org/10.48550/arXiv.2206.14537, arXiv:2206.14537.

Garofalo, R., Orena, S., Rafidi, K., Torchia, A., Stock, J., Hildebrandt, A., Coskran, T., Black, S., Brees, D., Wicks, J., McNeish, J., Coleman, K., 2003. Severe diabetes, age-dependent loss of adipose tissue, and mild growth deficiency in mice lacking akt2/pkbβ. J. Clin. Invest. 112 (2), 197–208. http://dx.doi.org/10.1172/JCI16885.

Geiß, C., Salas, E., Guevara-Coto, J., Régnier-Vigouroux, A., Mora-Rodríguez, R., 2011. Multistability in macrophage activation pathways and metabolic implications. Cell 146 (4), 633–644. http://dx.doi.org/10.3390/cells11030404.

Gillespie, D., 1976. A general method for numerically simulating the stochastic time evolution of coupled chemical reactions. J. Comput. Phys. 22 (4), 403–434. http://dx.doi.org/10.1016/0021-9991(76)90041-3.

Goetz, H., Melendez-Alvarez, J.R., Chen, L., Tian, X.-J., 2020. A plausible accelerating function of intermediate states in cancer metastasis. PLoS Comput. Biol. 16 (3), e1007682. http://dx.doi.org/10.1371/journal.pcbi.1007682.

González Pérez, A., Espinosa Angarica, V., Collado-Vides, J., Vasconcelos, A.T.R., 2009. From sequence to dynamics: the effects of transcription factor and polymerase concentration changes on activated and repressed promoters. BMC Mol. Biol. 10 (92), 1–15. http://dx.doi.org/10.1186/1471-2199-10-92.

Gupta, P., Fillmore, C., Jiang, G., Shapira, S., Tao, K., Kuperwasser, C., Lander, E., 2011. Stochastic state transitions give rise to phenotypic equilibrium in populations of cancer cells. Cell 146 (4), 633–644. http://dx.doi.org/10.1016/j.cell.2011.07.026.

Helfmann, L., Borrell, E., Schütte, C., Koltai, P., 2020. Extending transition path theory:Periodically driven and finite-time dynamics. J. Nonlinear Sci. 30 (6), 3321–3366. http://dx.doi.org/10.1007/s00332-020-09652-7.

Hörhold, F., Eisel, D., Oswald, M., Kolte, A., Röll, D., Osen, W., Eichmüller, S.B., König, R., 2020. Reprogramming of macrophages employing gene regulatory and metabolic network models. PLoS Comput. Biol. 16 (2), e1007657. http://dx.doi.org/10.1371/journal.pcbi.1007657.

Hu, X., Chen, J., Wang, L., Ivashkiv, L., 2007. Crosstalk among Jak-STAT, toll-like receptor, and ITAM-dependent pathways in macrophage activation. J. Leukoc. Biol. 82 (2), 237–243. http://dx.doi.org/10.1189/jlb.1206763.

Kim, K., Wang, J., 2007. Potential energy landscape and robustness of a gene regulatory network: Toggle switch. PLoS Comput. Biol. 3 (3), e60. http://dx.doi.org/10.1371/journal.pcbi.0030060.

Krombach, F., Münzing, S., Allmeling, A., Gerlach, J., Behr, J., Dörger, M., 1997. Cell size of alveolar macrophages: An interspecies comparison. Environ. Health Perspect. 105 (Suppl 5), 1261–1263. http://dx.doi.org/10.1289/ehp.97105s51261.

Lahmar, Q., Keirsse, J., Laoui, D., Movahedi, K., Van Overmeire, E., Van Ginderachter, J., 2016. Tissue-resident versus monocyte-derived macrophages in the tumor microenvironment. Biochim. Biophys. Acta - Rev. Cancer 1865 (1), 23–34. http://dx.doi.org/10.1016/j.bbcan.2015.06.009.

Lang, J., Nie, Q., Li, C., 2021. Landscape and kinetic path quantify critical transitions in epithelial-mesenchymal transition. Biophys. J. 120 (20), 4484–4500. http://dx.doi.org/10.1016/j.bpj.2021.08.043.

Li, X., Li, T., Li, C., Li, T., 2021. Uncovering the cell fate decision in lysis–lysogeny transition and stem cell development via Markov state modeling. J. Chem. Phys. 155 (24), 245101. http://dx.doi.org/10.1063/5.0070485.

Ma, J., Wei, K., Liu, J., Tang, K., Zhang, H., Zhu, L., Chen, J., Li, F., Xu, P., Liu, J., Fang, H., Tang, L., Wang, D., Zeng, L., Sun, W., Xie, J., Liu, Y., Huang, B., 2020. Glycogen metabolism regulates macrophage-mediated acute inflammatory responses. Nature Commun. 11 (1769), 1–16. http://dx.doi.org/10.1038/s41467-020-15636-8.

Malyshev, I., Malyshev, Y., 2015. Current concept and update of the macrophage plasticity concept: Intracellular mechanisms of reprogramming and M3 macrophage "switch" phenotype. Biomed. Res. Int. 2015 (341308), 2314–6133. http://dx.doi.org/10.1155/2015/341308.

Mantovani, A., Sica, A., Locati, M., 2005. Macrophage polarization comes of age. Immunity 23 (4), 344–346. http://dx.doi.org/10.1016/j.immuni.2005.10.001.

Martinez, F.O., Gordon, S., 2014. The M1 and M2 paradigm of macrophage activation: time for reassessment. F1000Prime Rep. 6, 13. http://dx.doi.org/10.12703/P6-13.

McKay, M., Beckman, R., Conover, W., 2000. A comparison of three methods for selecting values of input variables in the analysis of output from a computer code. Technometrics 42 (1), 55–61. http://dx.doi.org/10.1080/00401706.2000.10485979.

Metzner, P., Schütte, C., Vanden-Eijnden, E., 2009. Transition path theory for Markov jump processes. Multiscale Model. Simul. 7 (3), 1192–1219. http://dx.doi.org/10.1137/070699500.

Mishra, B., Athar, M., Mukhtar, M.S., 2021. Transcriptional circuitry atlas of genetic diverse unstimulated murine and human macrophages define disparity in population-wide innate immunity. Sci. Rep. 11 (1), 1–19. http://dx.doi.org/10.1038/s41598-021-86742-w.

Murray, P., 2017. Macrophage polarization. Annu. Rev. Physiol. 79, 541–566. http://dx.doi.org/10.1146/annurev-physiol-022516-034339.

Nickaeen, N., Ghaisari, J., Heiner, M., Moein, S., Gheisari, Y., 2019. Agent-based modeling and bifurcation analysis reveal mechanisms of macrophage polarization and phenotype pattern distribution. Sci. Rep. 9 (1), 12764. http://dx.doi.org/10.1038/s41598-019-48865-z.

Noé, F., Schütte, C., Vanden-Eijnden, E., Reich, L., Weikl, T., 2009. Constructing the equilibrium ensemble of folding pathways from short off-equilibrium simulations. Proc. Natl. Acad. Sci. 106 (45), 19011–19016. http://dx.doi.org/10.1073/pnas.0905466106.

O'Shea, J.J., Plenge, R., 2012. JAK and STAT signaling molecules in immunoregulation and immune-mediated disease. Immunity 36 (4), 542–550. http://dx.doi.org/10.1016/j.immuni.2012.03.014.

Palma, A., Jarrah, A.S., Tieri, P., Cesareni, G., Castiglione, F., 2018. Gene regulatory network modeling of macrophage differentiation corroborates the continuum hypothesis of polarization states. Front. Physiol. 9, 1659. http://dx.doi.org/10.3389/fphys.2018.01659.

Poh, A., Ernst, M., 2018. Targeting macrophages in cancer: from bench to bedside. Front. Oncol. 8 (49), 1–16. http://dx.doi.org/10.3389/fonc.2018.00049.

Porcheray, F., Viaud, S., Rimaniol, A., Léone, C., Samah, B., Dereuddre-Bosquet, N., Dormont, D., Gras, G., 2005. Macrophage activation switching: an asset for the resolution of inflammation. Front. Oncol. 142 (3), 481–489. http://dx.doi.org/10.1111/j.1365-2249.2005.02934.x.

Ralston, A., Rossant, J., 2005. Genetic regulation of stem cell origins in the mouse embryo. Clin. Genet. 68 (2), 106–112. http://dx.doi.org/10.1111/j.1399-0004.2005.00478.x.

Röblitz, S., Weber, M., 2013. Fuzzy spectral clustering by PCCA+: application to Markov state models and data classification. Adv. Data Anal. Classif. 7, 147–179. http://dx.doi.org/10.1007/s11634-013-0134-6.

Schaffer, A.E., Freude, K.K., Nelson, S.B., Sander, M., 2010. Nkx6 transcription factors and Ptf1a function as antagonistic lineage determinants in multipotent pancreatic progenitors. Dev. Cell 18 (6), 1022–1029. http://dx.doi.org/10.1016/j.devcel.2010.05.015.

Shapouri-Moghaddam, A., Mohammadian, S., Vazini, H., Taghadosi, M., Esmaeili, S.-A., Mardani, F., Seifi, B., Mohammadi, A., Afshari, J.T., Sahebkar, A., 2018. Macrophage plasticity, polarization, and function in health and disease. J. Cell Physiol. 233 (9), 6425–6440. http://dx.doi.org/10.1002/jcp.26429.

Sica, A., Mantovani, A., 2012. Macrophage plasticity and polarization: in vivo veritas. J. Clin. Invest. 122 (3), 787–795. http://dx.doi.org/10.1172/JCI59643.

Singhal, S., Stadanlick, J., Annunziata, M., Rao, A., Bhojnagarwala, P., O'Brien, S., Moon, E., Cantu, E., Danet-Desnoyers, G., Ra, H., Litzky, L., Akimova, T., Beier, U., Hancock, W., Albelda, S., Eruslanov, E., 2019. Human tumor-associated monocytes/macrophages and their regulation of t cell responses in early-stage lung cancer. Sci. Transl. Med. 11 (479), eaat1500. http://dx.doi.org/10.1126/scitranslmed.aat1500.

Smith, T.D., Tse, M.J., Read, E.L., Liu, W.F., 2016. Regulation of macrophage polarization and plasticity by complex activation signals. Integr. Biol. (Camb) 8 (9), 946–955. http://dx.doi.org/10.1039/c6ib00105j.

Stein, M., 1987. Large sample properties of simulations using Latin hypercube sampling. Technometrics 29 (2), 143–151. http://dx.doi.org/10.1080/00401706.1987.10488205.

Tse, M., Chu, B., Gallivan, C., Read, E., 2018. Rare-event sampling of epigenetic landscapes and phenotype transitions. PLoS Comput. Biol. 14 (8), e1006336. http://dx.doi.org/10.1371/journal.pcbi.1006336.

Vanden-Eijnden, E., 2010. Transition-path theory and path-finding algorithms for the study of rare events. Annu. Rev. Phys. Chem. 61, 391–420. http://dx.doi.org/10.1146/annurev.physchem.040808.090412.

Vellela, M., Qian, H., 2009. Stochastic dynamics and non-equilibrium thermodynamics of a bistable chemical system: the Schlögl model revisited. J. R. Soc. Interface 6 (39), 925–940. http://dx.doi.org/10.1098/rsif.2008.0476.

Wang, N., Liang, H., Zen, K., 2014. Molecular mechanisms that influence the macrophage M1–M2 polarization balance. Front. Immunol. 5, 614. http://dx.doi.org/10.3389/fimmu.2014.00614.

Waqas, S.F.H., Ampem, G., Rőszer, T., 2019. Analysis of IL-4/STAT6 signaling in macrophages. In: Badr, M. (Ed.), Nuclear Receptors. Methods in Molecular Biology, Vol. 1966. Springer, Humana, New York, NY, pp. 211–224. http://dx.doi.org/10.1007/978-1-4939-9195-2_17.

Wenta, N., Strauss, H., Meyer, S., Vinkemeier, U., 2008. Tyrosine phosphorylation regulates the partitioning of STAT1 between different dimer conformations. Proc. Natl. Acad. Sci. 105 (27), 9238–9243. http://dx.doi.org/10.1073/pnas.0802130105.

Yabo, Y., Niclou, S., Golebiewska, A., 2022. Cancer cell heterogeneity and plasticity: A paradigm shift in glioblastoma. Neuro-oncology 24 (5), 669–682. http://dx.doi.org/10.1093/neuonc/noac134.

Yang, Q., Guo, N., Zhou, Y., Chen, J., Wei, Q., Han, M., 2020. The role of tumor-associated macrophages (TAMs) in tumor progression and relevant advance in targeted therapy. Acta Pharm. Sin. B 10 (11), 2156–2170. http://dx.doi.org/10.1016/j.apsb.2020.04.004.

Yates, A., Callard, R., Stark, J., 2004. Combining cytokine signalling with T-bet and GATA-3 regulation in Th1 and Th2 differentiation: a model for cellular decision-making. J. Theoret. Biol. 231 (2), 181–196. http://dx.doi.org/10.1016/j.jtbi.2004.06.013.

Ye, L., Song, Z., Li, C., 2021. Landscape and flux quantify the stochastic transition dynamics for p53 cell fate decision. J. Chem. Phys. 154 (2), 025101. http://dx.doi.org/10.1063/5.0030558.

Zhao, C., Mirando, A.C., Sové, R.J., Medeiros, T.X., Annex, B.H., Popel, A.S., 2019. A mechanistic integrative computational model of macrophage polarization: Implications in human pathophysiology. PLoS Comput. Biol. 15 (11), e1007468. http://dx.doi.org/10.1371/journal.pcbi.1007468.

Zhou, J.X., Huang, S., 2011. Understanding gene circuits at cell-fate branch points for rational cell reprogramming. Trends Genet. 27 (2), 55–62. http://dx.doi.org/10.1016/j.tig.2010.11.002.